IEEE Open Journal of Antennas and Propagation

Received XX Month, XXXX; revised XX Month, XXXX; accepted XX Month, XXXX; Date of publication XX Month, XXXX; date of current version XX Month, XXXX.

Digital Object Identifier 10.1109/OJAP.2020.1234567

A Millimeter-Wave Scattering Channel Model for Indoor Human Activity Sensing

Mingqing Liu[1], Zhuangzhuang Cui[2], Yang Miao[2,3], Minseok Kim[4], Sofie Pollin[2]

[1]Department of Engineering, University of Cambridge, Cambridge CB3 0FA, UK
[2]Department of Electrical Engineering, KU Leuven, Leuven 3001, Belgium
[3]Faculty of Electrical Engineering, Mathematics and Computer Science, University of Twente, 7522, NB Enschede, The Netherlands
[4]Graduate School of Engineering, Niigata University, Japan

CORRESPONDING AUTHOR: Zhuangzhuang Cui (e-mail: zhuangzhuang.cui@kuleuven.be).

The work was supported in part by the MultiX and iSEE-6G projects under the Horizon Europe Research and Innovation programme with Grant Agreement No. 101192521, 101139291, respectively, and in part by KU Leuven through the project V.I.P. (H2020-MSCA-IF-2020) under Grant Agreement No. 101026885.

ABSTRACT In sixth-generation (6G) application scenarios like industry 5.0, augmented reality (AR), autonomous transportation, and eHealth, there is a growing demand for Human Activity Recognition (HAR). Meanwhile, with the deployment of millimeter-wave (mmWave) technologies in fifth-generation (5G) cellular communications, higher-resolution sensing becomes feasible. Utilizing mmWave for communication and HAR has garnered attention, necessitating accurate modeling of sensing channels. This paper proposes a mmWave scattering channel model for indoor HAR, which facilitates system design, optimization, and implementation. In the proposed model, we integrate primitive-based human body scattering where the human body is indicated by a set of primitives, and cluster-based environment scattering models, enabling detailed modeling of self-shadowing and double-bounce environment scattering. Additionally, we develop a simulation framework encompassing signal transmission, sensing channels, and processing, allowing adjustment of system parameters. Simulation results indicated by micro-Doppler signatures including multi-link effects show good agreements with measurements, validating the effectiveness of the proposed model. Meanwhile, the time consumption of the proposed simulation workflow for generating micro-Doppler signatures for most human activities is within 10 minutes.

INDEX TERMS mmWave ISAC, sensing channel, human activity recognition, self-shadowing check.

I. Introduction

INTERGRATED sensing and communication (ISAC) is envisioned as pivotal technology underpinning existing fifth-generation (5G) and forthcoming sixth-generation (6G) networks [1]. In various vertical application scenarios of 6G such as industry 4.0, augmented reality (AR), autonomous transportation, and eHealth, leveraging existing communication signals and systems for the implementation of sensing functions is considered as one key enabler because of the potential benefits of spectrum reuse and hardware integration [2]. Within the aforementioned application landscapes, accurate human activity recognition (HAR) is demanding to provide smart human assistance, e.g., AR human-body interaction, pedestrian detection in transportation, and falling detection for elderly care [3]. Besides, with the standardization of millimeter-wave (mmWave) technology in 5G, it becomes feasible to conduct high-resolution sensing using communication signals/systems [4]. However, developing a practical human-centered scattering (HCS) channel model for HAR that balances accuracy and efficiency in mmWave bands remains challenging. To address this, this paper proposes an indoor mmWave scattering channel model for HAR applications, which integrates trajectory-driven deterministic human activity with stochastic environment modeling.

HAR in the mmWave bands has attracted a great deal of attention, bringing applications such as finger gesture recognition by Google [5], mmWave radar products for human detection by Texas Instruments [6], as well as human tracking, localization, and activity recognition in the context of ISAC. On the other hand, developing channel models

and simulators for HAR is essential for generating data to support further research on recognition algorithm design, real ISAC system development, optimization, and more. However, modeling scattering from a moving human body is inherently difficult due to the following reasons: i) the human body has complex structures and rich reflection points, ii) the movement of the human body is coordinated but complicated depending on the type of motion, and iii) human tissues on different body parts have various reflection characteristics; from where we identify two key factors for modeling the HCS channel: the radar cross section (RCS) of the human body and the trajectory of its movement. Two HAR sensing channel modeling methods have been developed and widely adopted in existing research to address the above issues: primitive-based [7], [8] and ray tracing-based model [9].

For primitive-based models, each body part is modeled as primitives, such as a sphere, ellipsoid, etc., and the RCS is calculated analytically [10]. The trajectory of each part is determined from the data captured by specific systems, i.e., motion capture (MOCAP) system, Kinect sensor, etc [11], [12]. Generally, only the line of sight (LoS) channel between each body part and the transceiver is considered, and the total scatterer number in the channel depends on the predefined primitive number. In [13], a Kinect-based human micro-Doppler simulator with a human body scattering model has been developed for radar applications, where the human body is divided into 17 parts represented by primitive shapes for RCS calculation, and the trajectory is derived from data captured by Kinect sensors. Micro-Doppler signatures for various human activities can be obtained from the simulator by short-time Fourier transform (STFT) analysis. A similar modeling and simulation flow is conducted in [8] with bistatic radar, using the trajectory derived from the existing MOCAP database. The above simulators lack the configuration of transceiver architectures, making it difficult for them to adapt to ISAC systems. In [7] and [14], simulators are designed for passive WiFi scenarios, integrating the packet structure of the IEEE 802.11 standards (IEEE 802.11g, n, and ad) with specially developed signal processing methods to extract micro-Doppler signatures. Yet, they do not account for environmental reflections in their models.

For the ray-tracing-based model, a 3-dimensional (3D) model of the human body is used and meshed, while the trajectory of each part is also captured from MCAP. Using shooting and bouncing rays to simulate the propagation and interaction of rays with the human body, RCS is calculated by physical optics. Many studies on channel and signal modeling based on ray tracing for moving humans have been conducted using commercial simulators like Wireless InSite, as well as self-built lightweight simulators [9], [15], [16]. Due to the precise object segmentation and the interactions of multiple rays with objects in the given scenario, ray-tracing-based models incorporate reflections from environmental components and enable more accurate channel modeling, inherently including self-shadowing effects among different human body parts. However, time/computing efficiency is a significant bottleneck for ray-tracing-based models, as the simulator may require trajectory data to be imported frame by frame for various human activities [16]. Some researchers have also explored quasi-deterministic ray tracing modeling [17] and primitive-based models with environmental scatterers [18]–[20] to balance efficiency and accuracy. Still, there is a gap in developing comprehensive channel models and flexibly adjustable simulators for HAR applications.

To conclude, the primitive-based model is time-saving and provides a micro-Doppler signature that aligns reasonably with real-world situations; however, it neglects self-shadowing among human body parts and multiple reflections from interactions with the environment. In contrast, the ray-tracing-based model can achieve high accuracy and automatically accounts for self-shadowing and multi-reflections. Nevertheless, it is highly time-consuming, computationally expensive, and challenging to apply in dynamic scenarios. To reap benefits from both methods, this paper aims to establish a refined sensing channel model that integrates a trajectory-driven, primitive-based human body scattering model with a stochastic, cluster-based environment scattering model. Additionally, we added a self-shadowing checking procedure to simulate realistic human movement. Together, these elements contribute to achieving a balance between accuracy and efficiency. Furthermore, to accommodate modeling the ISAC system with shared communication-centric waveform, we build a complete simulation framework with flexible antenna configuration, transmitter/receiver deployment, waveform generation, signal scattering, receiving, and modeling. After STFT analysis, a key output of this simulator is the micro-Doppler signature, which reflects various human motions. We compared the generated micro-Doppler signatures with real-world measurements, validating the effectiveness of the proposed model.

The contributions of this paper are:

C1) We propose a refined channel model for human activity sensing with the combination of a primitive-based human model and cluster-based scattering model. The proposed channel model considers self-shadowing and double-bounce environment scattering. More importantly, the model allows for fast simulation, as 10 minutes is more than enough for simulating most various human activities using personal computers.

C2) We build a simulator for human activity sensing including transmitting signal and topology, sensing channel, and receiving signal and radar processing, where system parameters such as antenna pattern, waveform, etc., can be flexibly adjusted. Using the micro-Doppler signature as a key metric, simulation results with the proposed channel model are in generally good agreement with the corresponding measurements.

The remainder of this paper is organized as follows. In Section II, we built a 3D geometrical illustration for indoor

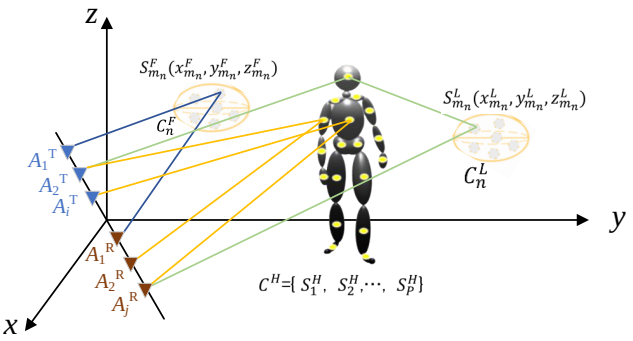

FIGURE 1. 3D geometrical model for human activity sensing under monostatic deployment.

wave propagation under monostatic, bistatic, and multi-static deployments. In Section III, we formulated the channel model including channel response considering scattering from the human body, scattering from static scatterers based on the cluster model, and double-bounce scattering. Self-shadowing checking method and micro-Doppler processing are also introduced in Sec. III. In Section IV, we present the simulation implementation details and show the micro-Doppler signatures with various human motions through simulations. We also introduce a human activity measurement dataset, where we demonstrate that the simulation results are in good agreement with the measurement. Finally, we concluded the paper in Section V.

II. 3D Geometry-based Representation

This section gives a 3D geometrical illustration for indoor wave propagation specifically HCS channels under three deployment topologies: monostatic, bistatic, and multi-static. Aiming at HAR, we borrowed ideas from the 3D non-stationary geometry-based stochastic model (GBSM), where the human body is simplified as a set of moving scatterers, and the background environment is modeled by clusters following stochastic distributions. Both the transmitter (Tx) and receiver (Rx) are embedded with antenna arrays and phase-shift beamforming is applied.

A. Monostatic Deployment

Figure 1 depicts the 3D geometrical indoor wave propagation scenario with a moving human. The presented system has N_{T} antennas at Tx and N_{R} antennas at Rx. $A_i^{\mathrm{T}}(i = 1, 2, .., N_{\mathrm{T}})$ denotes transmit antenna i, and $A_j^{\mathrm{R}}(j = 1, 2, .., N_{\mathrm{R}})$ denotes receive antenna j. Scatterers in the whole simulated setting are grouped in different clusters, categorized as i) clusters representing the background environment (e.g., walls, ceilings, window), denoted by $C_n(n = 1, 2, .., N(t))$ and ii) clusters indicating human body parts C^{H}. There are $N(t)$ background environment clusters with M scatterers $S_{m_n}(m = 1, 2, .., M)$ each, and $N^{\mathrm{B}}(t) = N(t)M$ denotes the total scatterers. Each scatterer specifies a ray from Tx to Rx and the birth-death process is applied to emulate the visibility of clusters to the Tx at time instant t. C^{H} includes $P(t)$ moving scatterers $S_p^{\mathrm{H}}(p = 1, 2, .., P(t))$, where $P(t)$ is determined by the predefined number of human body parts and varies due to self-shadowing at each time instant t. With monostatic deployment, Tx and Rx are co-located at a fixed position as in Fig. 1. The moving trajectory of S_p^{H} is set as a known set $\mathcal{T}(t) = \left\{(x_p^{\mathrm{H}}(t), y_p^{\mathrm{H}}(t), z_p^{\mathrm{H}}(t))|p = 1, 2, ..., P(t)\right\}$ along time, which is obtained from existing datasets collected by MOCAP systems. Different trajectory sets are formed for various human activities.

Moreover, a two-bounce propagation mechanism is adopted, where background clusters consist of a pair of sub-clusters, i.e., first-bounce from Tx side to C_n^{F} and last-bounce from C_n^{L} to Rx side. Hence, there are five components contained in the proposed model: i) single-bounce component with path Tx $\rightarrow C_n \rightarrow$ Rx (with C^{F} and C^{L} considered as a whole); ii) single-bounce component with path Tx $\rightarrow C^{\mathrm{H}} \rightarrow$ Rx; iii) double-bounce component with path Tx $\rightarrow C_n^{\mathrm{F}} \rightarrow C_n^{\mathrm{L}} \rightarrow$ Rx; iv) double-bounce component with path Tx $\rightarrow C_n^{\mathrm{F}} \rightarrow C^{\mathrm{H}} \rightarrow$ Rx; v) double-bounce component with path Tx $\rightarrow C^{\mathrm{H}} \rightarrow C_n^{\mathrm{L}} \rightarrow$ Rx. To build channel models, two geometric information elements are first determined for the above links: path lengths and angles, i.e., angle of arrival (AOA), angle of departure (AOD), elevation angle of arrival (EOA), and elevation angle of departure (EOD). Under monostatic case, we neglect the position differences in Tx and Rx antenna array and links of each pair of transmitting and receiving waves are assumed to share the same path lengths and angles. For instance, the path length of the single-bounce component including $S_{m_n}^{\mathrm{F/L}}$ at time t is

$$d_{m_n}^{\mathrm{B}}(t) = 2\left\|\mathbf{A} - \mathbf{S}_{m_n}^{\mathrm{F/L}}(t)\right\|, \tag{1}$$

where $\mathbf{A}$ denotes the 3D position vector (x, y, z) of monostatic Tx/Rx with assumption of $\mathbf{A} = \mathbf{A}_i^{\mathrm{T}} = \mathbf{A}_j^{\mathrm{R}}$, $\mathbf{S}_{m_n}^{\mathrm{F/L}}$ is the position vector of $S_{m_n}^{\mathrm{F/L}}$, and $\|\cdot\|$ indicates Euclidean norm operation. The AOA/AOD and EOA/EOD are expressed by

$$\begin{aligned}\varphi_{m_n}^{\mathrm{B,AOA}} &= \varphi_{m_n}^{\mathrm{B,AOD}} = \arctan\frac{y - y_{m_n}^{\mathrm{F/L}}}{x - x_{m_n}^{\mathrm{F/L}}} \\ \varphi_{m_n}^{\mathrm{B,EOA}} &= \varphi_{m_n}^{\mathrm{B,EOD}} = \arcsin\frac{z - z_{m_n}^{\mathrm{F/L}}}{\left\|\mathbf{A} - \mathbf{S}_{m_n}^{\mathrm{F/L}}\right\|}\end{aligned}. \tag{2}$$

Correspondingly, we can derive path lengths $d_p^{\mathrm{H}}(t)$ and angles $\varphi_p^{\mathrm{AOA}}, \varphi_p^{\mathrm{AOD}}, \varphi_p^{\mathrm{EOA}}, \varphi_p^{\mathrm{EOD}}$ of single-bounce links involving human body cluster C^{H} in a similar manner.

For double-bounce links, path lengths of components iii)-v) illustrated above are expressed below, respectively:

$$\begin{aligned}d_{m_n}^{\mathrm{BB}}(t) &= \left\|\mathbf{A} - \mathbf{S}_{m_n}^{\mathrm{F}}(t)\right\| + \left\|\mathbf{A} - \mathbf{S}_{m_n}^{\mathrm{L}}(t)\right\| \\ &\quad + \left\|\mathbf{S}_{m_n}^{\mathrm{F}}(t) - \mathbf{S}_{m_n}^{\mathrm{L}}(t)\right\| \\ d_{m_n,p}^{\mathrm{BH}}(t) &= \left\|\mathbf{A} - \mathbf{S}_{m_n}^{\mathrm{F}}(t)\right\| + \left\|\mathbf{A} - \mathbf{S}_p^{\mathrm{H}}(t)\right\| \\ &\quad + \left\|\mathbf{S}_{m_n}^{\mathrm{F}}(t) - \mathbf{S}_p^{\mathrm{H}}(t)\right\| \\ d_{m_n,p}^{\mathrm{HB}}(t) &= \left\|\mathbf{A} - \mathbf{S}_p^{\mathrm{H}}(t)\right\| + \left\|\mathbf{A} - \mathbf{S}_{m_n}^{\mathrm{L}}(t)\right\| \\ &\quad + \left\|\mathbf{S}_p^{\mathrm{H}}(t) - \mathbf{S}_{m_n}^{\mathrm{L}}(t)\right\|\end{aligned}, \tag{3}$$

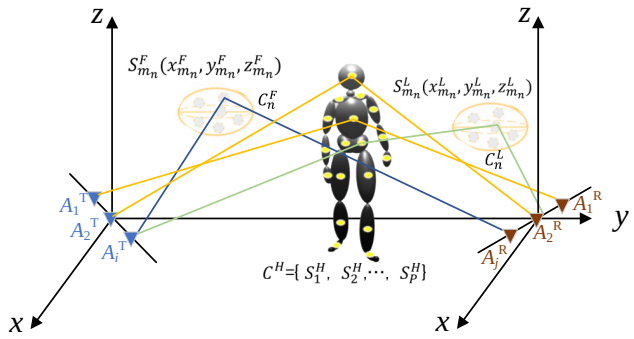

FIGURE 2. 3D geometrical model for human activity sensing under bistatic deployment.

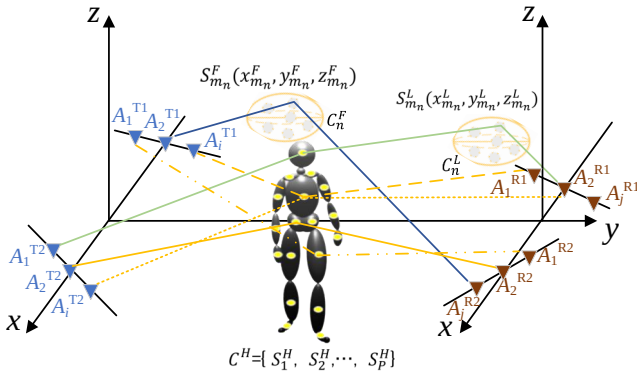

FIGURE 3. 3D geometrical model for human activity sensing under multistatic deployment.

where the superscript $\{\mathrm{BB}, \mathrm{BH}, \mathrm{HB}\}$ indicates paths including $C_n^{\mathrm{F}} \rightarrow C_n^{\mathrm{L}}, C_n^{\mathrm{F}} \rightarrow C^{\mathrm{H}}$, and $C^{\mathrm{H}} \rightarrow C_n^{\mathrm{L}}$, aligning with components iii)-v). $\mathbf{S}^{\mathrm{F}}_{m_n}, \mathbf{S}^{\mathrm{L}}_{m_n}, \mathbf{S}^{\mathrm{H}}_{p}$ denote the position vector of scatterers in $C_n^{\mathrm{F}}, C_n^{\mathrm{L}}, C^{\mathrm{H}}$, respectively. Meanwhile, the AOA/EOA and AOD/EOD are determined by relative directions of first scattering from Tx and last scattering to Rx, correspondingly. With the time-varying path lengths of wave propagation, the Doppler modulation introduced by human moving will be reflected in the backscattering signal, including the effect of background environment scattering.

B. Bistatic Deployment

Figure 2 depicts the 3D geometrical model for HCS under bistatic deployment, where Tx and Rx are spatially separated. Each transmitting antenna $A_i^{\mathrm{T}}(i = 1, 2, ..., N_{\mathrm{T}})$ is located at $\mathbf{A}_i^{\mathrm{T}}(x_i^{\mathrm{T}}, y_i^{\mathrm{T}}, z_i^{\mathrm{T}})$ and receiving antenna $A_j^{\mathrm{R}}(j = 1, 2, ..., N_{\mathrm{R}})$ at $\mathbf{A}_j^{\mathrm{R}}(x_j^{\mathrm{R}}, y_j^{\mathrm{R}}, z_j^{\mathrm{R}})$. Same as the monostatic scenario, $N^{\mathrm{B}}(t)$ scatterers indicate the indoor environment, and $P(t)$ moving scatterers represent the human body. Path lengths of components i)-v) should consider different locations of each pair of Tx/Rx antenna denoted with subscription ij, which are given as follows, respectively:

$$
\begin{aligned}
d^{\mathrm{B}}_{ij,m_n} &= \left\|\mathbf{A}_i^{\mathrm{T}} - \mathbf{S}^{\mathrm{F/L}}_{m_n}(t)\right\| + \left\|\mathbf{A}_j^{\mathrm{R}} - \mathbf{S}^{\mathrm{F/L}}_{m_n}(t)\right\| \\
d^{\mathrm{H}}_{ij,p}(t) &= \left\|\mathbf{A}_i^{\mathrm{T}} - \mathbf{S}^{\mathrm{H}}_{p}(t)\right\| + \left\|\mathbf{A}_j^{\mathrm{R}} - \mathbf{S}^{\mathrm{H}}_{p}(t)\right\| \\
d^{\mathrm{BB}}_{ij,m_n}(t) &= \left\|\mathbf{A}_i^{\mathrm{T}} - \mathbf{S}^{\mathrm{F}}_{m_n}(t)\right\| + \left\|\mathbf{A}_j^{\mathrm{R}} - \mathbf{S}^{\mathrm{L}}_{m_n}(t)\right\| \\
&\quad + \left\|\mathbf{S}^{\mathrm{F}}_{m_n}(t) - \mathbf{S}^{\mathrm{L}}_{m_n}(t)\right\| \\
d^{\mathrm{BH}}_{ij,m_n p}(t) &= \left\|\mathbf{A}_i^{\mathrm{T}} - \mathbf{S}^{\mathrm{F}}_{m_n}(t)\right\| + \left\|\mathbf{A}_j^{\mathrm{R}} - \mathbf{S}^{\mathrm{H}}_{p}(t)\right\| \\
&\quad + \left\|\mathbf{S}^{\mathrm{F}}_{m_n}(t) - \mathbf{S}^{\mathrm{H}}_{p}(t)\right\| \\
d^{\mathrm{HB}}_{ij,m_n p}(t) &= \left\|\mathbf{A}_i^{\mathrm{T}} - \mathbf{S}^{\mathrm{H}}_{p}(t)\right\| + \left\|\mathbf{A}_j^{\mathrm{R}} - \mathbf{S}^{\mathrm{L}}_{m_n}(t)\right\| \\
&\quad + \left\|\mathbf{S}^{\mathrm{H}}_{p}(t) - \mathbf{S}^{\mathrm{L}}_{m_n}(t)\right\|
\end{aligned}
\tag{4}
$$

where the superscript $\{\mathrm{B}, \mathrm{H}\}$ indicates single-bounce paths involving $C_n^{\mathrm{F/L}}$ and C^{H}, respectively. To avoid duplication, we only specify the angles of the component ii) as below

$$
\begin{aligned}
\varphi^{\mathrm{AOA}}_{ij,p} &= \arctan\frac{y_j^{\mathrm{R}} - y_p^{\mathrm{H}}}{x_j^{\mathrm{R}} - x_p^{\mathrm{H}}}, \varphi^{\mathrm{EOA}}_{ij,p} = \arcsin\frac{z_j^{\mathrm{R}} - z_p^{\mathrm{H}}}{\left\|\mathbf{A}_j^{\mathrm{R}} - \mathbf{S}_p^{\mathrm{H}}\right\|} \\
\varphi^{\mathrm{AOD}}_{ij,p} &= \arctan\frac{y_i^{\mathrm{T}} - y_p^{\mathrm{H}}}{x_i^{\mathrm{T}} - x_p^{\mathrm{H}}}, \varphi^{\mathrm{EOD}}_{ij,p} = \arcsin\frac{z_i^{\mathrm{T}} - z_p^{\mathrm{H}}}{\left\|\mathbf{A}_i^{\mathrm{T}} - \mathbf{S}_p^{\mathrm{H}}\right\|}
\end{aligned}
\tag{5}
$$

C. Multistatic Deployment

Considering networked sensing applications, we also depict a multistatic deployment as in Fig. 3, where two transmitters, i.e., Tx_1 and Tx_2, and two receivers, i.e., Rx_1 and Rx_2 are included. Each antenna from the Tx/Rx arrays is denoted by A_i^{T1}, A_i^{T2}, A_j^{R1}, and A_j^{R2}, respectively. All transmitters and receivers are spatially separated. Hence, there are four propagation channels: i) $\mathrm{Tx}_1 \rightarrow \mathrm{Rx}_1$, ii) $\mathrm{Tx}_1 \rightarrow \mathrm{Rx}_2$, iii) $\mathrm{Tx}_2 \rightarrow \mathrm{Rx}_1$, and iv) $\mathrm{Tx}_2 \rightarrow \mathrm{Rx}_2$. The scatterers indicating indoor environments and a moving human body are the same as the above two deployments. Moreover, links between Tx/Rx and background scatterers, moving scatterers with single-bounce propagation, and moving scatterers with double-bounce propagation should be established for the four channels, respectively. We abbreviated the geometric expressions here as the path lengths and angles of different links for each pair of Tx/Rx have the same formulations under bistatic deployment.

III. Channel Modeling and Micro-Doppler Extraction

In this section, channel modeling based on geometry representations is conducted considering monostatic, bistatic, and multistatic deployments. We first present the generation and evolution of background scatterers to determine their positions. Then, we detail the formulation of channel response by defining time delay, Doppler shift, attenuation, and antenna pattern. Further, we develop a self-shadowing checking process for simulating blockage among different human body parts while human moving. Finally, we introduce STFT analysis for micro-Doppler signature extraction.

A. Generation and Evolution of Background Scatterers

Before modeling the channel response, we first generate scatterers in the sensing channel model. For the moving scatterers indicating the human body, the trajectory, i.e., positions of each scatterer at instant t are determined from the existing database by the MOCAP system. For scatterers indicating other environmental objects, the initial cluster locations are generated first by distance $\overline{d}$ from Tx/Rx to the center of background clusters, which is assumed to be non-negative random variables following exponential distribution within an interior room indicated by $L \times W \times H$ (length by width by height of the room). Angles $\overline{\varphi}_E, \overline{\varphi}_A$ are assumed to be with Gaussian distributions. We then adopted the Gaussian scatter density model (GSDM) which collects scatterers with azimuth angles, elevation angles, and distances similar to the detection of Tx and Rx for the distribution of scatterers within clusters [21]. In GSDM, the distance and angle parameters between the scatterers and Tx / Rx follow the ellipsoid Gaussian scattering distribution and the scattering coordinates centering on the origin of the coordinates can be modeled as [22]

$$p(x', y', z') = \frac{\exp\left(-\frac{x'^2}{2\varepsilon_{DS}^2} - \frac{y'^2}{2\varepsilon_{AS}^2} - \frac{z'^2}{2\varepsilon_{ES}^2}\right)}{(2\pi)^{3/2}\varepsilon_{DS}\varepsilon_{AS}\varepsilon_{ES}}. \tag{6}$$

where $\varepsilon_{DS}, \varepsilon_{AS}, \varepsilon_{ES}$ denote the standard derivations of the Gaussian distributions and characterize delay spread, azimuth angle spread, and elevation angle spread of the cluster, respectively. Given a room size, clusters are generated randomly with the spherical coordinates of the cluster center denoted as $(\overline{d}, \overline{\varphi}_E, \overline{\varphi}_A)$. Then, the positions of scatterers (x, y, z) centering around the cluster center are stated as

$$\begin{bmatrix} x \\ y \\ z \end{bmatrix} = \begin{bmatrix} \cos(\bar{\varphi}_A) & -\sin(\bar{\varphi}_A) & 0 \\ \sin(\bar{\varphi}_A) & \cos(\bar{\varphi}_A) & 0 \\ 0 & 0 & 1 \end{bmatrix} \begin{bmatrix} \cos(\bar{\varphi}_E) & 0 & -\sin(\bar{\varphi}_E) \\ 0 & 1 & 0 \\ \sin(\bar{\varphi}_E) & 0 & \cos(\bar{\varphi}_E) \end{bmatrix} \begin{bmatrix} x' - \bar{d} \\ y' \\ z' \end{bmatrix}. \tag{7}$$

After generating the background clusters and scatterers, the birth-death process is applied to emulate the visibility of background clusters at each time instant $(t, t + \Delta t, t + 2\Delta t, ...)$. Unlike the birth-death process used in most general channel models where the Tx, Rx, and clusters are randomly moving, only the human body is modeled as a moving component in this work. Thus, we use the birth-death process to simulate the potential blockage to background clusters due to the human body movement. Moreover, the changes of background clusters are relatively slow compared to the human body cluster, and a simplified Poisson process is considered to describe the generation and extinction of such background clusters. Following the algorithm proposed in [21], each cluster is assigned with a birth rate λ_{B} and death rate λ_{D}, and remains from t to $t + \Delta t$ with the probability

$$P_{\mathrm{remain}} = \exp\left[-\lambda_D P_{\mathrm{H}} v_{\mathrm{H}} \Delta t\right], \tag{8}$$

where P_{H} is the ratio of the human cluster number to the total background cluster number and v_{H} is the mean velocity of human body movement. Then, at $t+\Delta t$, the new clusters are generated following the Poisson distribution with expectation

$$\mathbf{E}\{N_{\mathrm{new}}\} = \frac{\lambda_B}{\lambda_D}(1 - P_{\mathrm{remain}}) \tag{9}$$

The above process is applied to both clusters C^{F} and C^{L}.

B. Channel Response

The channel transfer function (CTF) matrix is expressed by a $N_{\mathrm{T}} \times N_{\mathrm{R}}$ matrix $\mathbf{H}_{N_{\mathrm{T}} \times N_{\mathrm{R}}} = [H_{ij}(t, f')]_{N_{\mathrm{T}} \times N_{\mathrm{R}}}$. Based on the geometric model presented above, we express the wave propagation from antenna A_i^{T} to antenna A_j^{R} as

$$\begin{aligned} H_{ij}(t, f') = {} & H_{ij}^{\mathrm{B}}(t, f') + H_{ij}^{\mathrm{H}}(t, f') \\ & + H_{ij}^{\mathrm{BB}}(t, f') + H_{ij}^{\mathrm{BH}}(t, f') + H_{ij}^{\mathrm{HB}}(t, f'). \end{aligned} \tag{10}$$

Corresponding to the components illustrated in the geometric model part, the complete channel response $H_{ij}(t, f')$ consists of five parts. $H_{ij}^{\mathrm{B}}(t, f')$ and $H_{ij}^{\mathrm{H}}(t, f')$ denote channel of single-bounce from background and human body scatterers, respectively; $H_{ij}^{\mathrm{BB}}(t, f')$, $H_{ij}^{\mathrm{BH}}(t, f')$, and $H_{ij}^{\mathrm{HB}}(t, f')$ represent double-bounce among background scatterers, background and human body scatterers, and human body and background scatterers, respectively. For each component, the total contribution of various scatterers should be considered. Thus, H_{ij}^{B} related to time and frequency is defined as

$$\begin{aligned} H_{ij}^{\mathrm{B}}(t, f') = {} & \sum_{n=1}^{N(t)} \sum_{m=1}^{M} G_{ij,m_n} a_{ij,m_n}^{\mathrm{B}} \\ & \times \exp\left\{-2\pi j (f' + f_c) \tau_{ij,m_n}^{\mathrm{B}}(t)\right\} \end{aligned}, \tag{11}$$

where f_c represent the carrier frequency, respectively; G_{ij,m_n} denotes antenna pattern function and a_{ij,m_n}^{B} is the scatterer reflectivity related channel gain; $\tau_{ij,m_n}^{\mathrm{B}}$ is the distance related propagation delay. The above parameters will be defined and discussed in detail below. For the moving human body, Doppler shift is included in the channel response, and H_{ij}^{H} is expressed as

$$\begin{aligned} H_{ij}^{\mathrm{H}}(t, f') = {} & \sum_{p=1}^{P(t)} G_{ij,p} a_{ij,p}^{\mathrm{H}}(t) \\ & \times \exp\left\{2\pi j \left[t f_{ij,p}^{\mathrm{H}}(t) - (f' + f_c)\tau_{ij,p}^{\mathrm{H}}(t)\right]\right\} \end{aligned}, \tag{12}$$

where $f_{ij,p}^{\mathrm{H}}(t)$ is the Doppler shift induced by the radial velocity of moving human body parts. $P(t)$ is the instantaneous total number of paths between Tx and Rx scattered by human scatterers. Considering self-shadowing effect, we use an index set $\mathcal{C}(t)$ to indicate scatterers that are not blocked by other body parts, and $P(t)$ is the set size.

For H_{ij}^{BB}, only delay in Eq. (11) needs to be repleced by $\tau_{ij,m_n}^{\mathrm{BB}}$, while for H_{ij}^{BH} and H_{ij}^{HB}, Doppler shift $f_{ij,m_n p}^{\mathrm{BH}}$ and $f_{ij,m_n p}^{\mathrm{HB}}$ in addition to delays should be considered. Besides, we assume the total number of clusters is divided equally for first-bounce and last-bounce scattering, respectively. Thus, the total number of scatterers considered in the human body

related double-bounce link is $\frac{N_{\mathrm{B}}(t)P(t)}{2}$. In the following, we define the aforementioned parameters, i.e., antenna pattern, delay, Doppler shift, and channel gain in detail.

1) Antenna Pattern

The antenna pattern function is related to the azimuth and elevation angles of transmitted beam and receiving beam to the antenna. For example, $G_{ij,p}$ in Eq. (12) is expressed as

$$G_{ij,p} = \begin{bmatrix} F_{i,V}^{T}\left(\varphi_{ij,p}^{\mathrm{EOD}}, \varphi_{ij,p}^{\mathrm{AOD}}\right) \\ F_{i,H}^{T}\left(\varphi_{ij,p}^{\mathrm{EOD}}, \varphi_{ij,p}^{\mathrm{AOD}}\right) \end{bmatrix}^{T} \begin{bmatrix} e^{j\Phi_{ij,p}^{\mathrm{VV}}} & \sqrt{\kappa}e^{j\Phi_{ij,p}^{\mathrm{VH}}} \\ \sqrt{\kappa}e^{j\Phi_{ij,p}^{\mathrm{HV}}} & e^{j\Phi_{ij,p}^{\mathrm{HH}}} \end{bmatrix} \begin{bmatrix} F_{j,V}^{R}\left(\varphi_{ij,p}^{\mathrm{EOA}}, \varphi_{ij,p}^{\mathrm{AOA}}\right) \\ F_{j,H}^{R}\left(\varphi_{ij,p}^{\mathrm{EOA}}, \varphi_{ij,p}^{\mathrm{AOA}}\right) \end{bmatrix}, \tag{13}$$

where $F_{i,V(H)}^{T}$ and $F_{j,V(H)}^{R}$ denote antenna patterns of antennas A_i^{T} and A_j^{R} for vertical (horizontal) polarizations, respectively, $\{\cdot\}^T$ indicates transposition process, κ is the cross-polarization power ratio, and $\Phi_{ij,p}^{\mathrm{VV}}$, $\Phi_{ij,p}^{\mathrm{VH}}$, $\Phi_{ij,p}^{\mathrm{HV}}$, and $\Phi_{ij,p}^{\mathrm{HH}}$ are uniformly distributed random phases over $(-\pi, \pi)$.

2) Delay and Doppler

The propagation delays $\tau_Y^X(t)$, where the superscript $X \in \{\mathrm{B}, \mathrm{H}, \mathrm{BB}, \mathrm{BH}, \mathrm{HB}\}$ and subscript $Y \in \{\{ij, m_n\}, \{ij, p\}, \{ij, m_n\}, \{ij, m_n p\}, \{ij, m_n p\}\}$ relating to Eq. (4) are presented as

$$\tau_Y^X(t) = \frac{d_Y^X(t)}{c_0}, \tag{14}$$

where c_0 is the speed of light. Meanwhile, Doppler shift is calculated by the radial moving velocity of each body part relative to the transceiver as

$$f_{ij,p}^{\mathrm{H}}(t) = \frac{2v_{ij,p}^{\mathrm{H}}(t)f_c}{c_0}\cos(\beta/2), \tag{15}$$

where β is the bi-static angle, and $v_{ij,p}^{\mathrm{H}}$ is obtained through the human moving trajectory, by calculating relative position vector change at each time slot.

3) Channel Gain

According to the free-space path-loss model, the channel gain a in the above equations is related to the distance between scatter and transceiver, propagation effects, etc. Moreover, RCS estimation of the human body is crucial for the HCS model. In our proposed model, we represent different body parts using primitives, i.e., a sphere for the head and ellipsoids for the arms, to embody a human skeleton model. This allows us to apply analytical RCS calculations for each primitive, enabling accurate RCS estimation for individual body parts. Thus, we formulate $a_{ij,p}^{\mathrm{H}}(t)$ as

$$a_{ij,p}^{\mathrm{H}}(t) = \frac{G_{ij,p}(t)\sqrt{\sigma_{ij,p}^{\mathrm{H}}(t)}}{\left\|\mathbf{A}_i^{\mathrm{T}} - \mathbf{S}_p^{\mathrm{H}}(t)\right\| \cdot \left\|\mathbf{A}_j^{\mathrm{R}} - \mathbf{S}_p^{\mathrm{H}}(t)\right\|}, \tag{16}$$

where $G_{ij,p}(t)$ indicates antenna gain as in Eq. (13), and $\sigma_{ij,p}^{\mathrm{H}}(t)$ indicates RCS of p-th scatterer (i.e., primitive) relative to antennas A_i^{T} and A_j^{R} under single-bounce propagation, which is depicted as Eq. (17), with a_p, b_p, c_p denoting radii along the x, y, z axis of ellipsoid. In Eq. (17), time-varying AOA/EOA/AOD/EOD are also included. Meanwhile, for background clusters, we assume RCS of each scatterer remains the same as a constant.

C. Self-Shadowing Effects

To approach the realistic situation, we also consider the self-shadowing among different human body parts while a human is moving. As mentioned above, various human body parts are represented by primitives with different sizes. As long as the scatterer considered for human simulation has a specific size, we could leverage methods to check whether the wave scattered by a specific body part would be blocked by other body parts to the receiver under motions. The checking principle is simple: given a LoS link between a primitive center (i.e., the position of the scatterer) on the human body and the transceiver, if the link intersects with any other primitives (i.e., mainly ellipsoid) indicating other body parts, we determine this link is self-shadowed. Then, the contribution of this link to the backscattering signal is removed. Algorithm 1 depicts the self-shadowing checking process. $\mathcal{P}$ indicates a set of each ellipsoid, where columns $1 \sim 3$ store position and columns $4 \sim 6$ store radii of ellipsoid along x, y, z axis, respectively. To accelerate the checking process, we first use the function "ComputeBox()" to calculate the boundary box of each ellipsoid. As long as there is an intersection between the current ellipsoid and boxes of other ellipsoids, checking for an intersection with the ellipsoid is required. If an intersection exists, the current scatterer's contribution is removed.

D. Micro-Doppler Analysis

As there are static objects considered in the modeling, we should first remove the static reflections from the total channel response for human activity sensing. Given a symbol or packet transmission time as T_c, we sample the channel response in time, and index $q = 1, ..., Q$ is denoted as discrete time instants. Hence, channel response can be represented as $H(q, f'), t = qT_c$. For signal processing, we compute channel impulse response $h(t, \tau')$ by taking the inverse Fourier transform (IFFT) of $H(t, f')$. Then, the background-related channel response is estimated as

$$\overline{h}(t, \tau') = \frac{1}{Q}\sum_{q=1}^{Q}|h(t, \tau')|, \tag{18}$$

which means the time average of channel amplitude within a window of Q samples [14]. Then, the channel response amplitude after subtracting the background is depicted as

$$|\hat{h}(t, \tau')| = \max(|h(t, \tau')| - \overline{h}(t, \tau'), 0). \tag{19}$$

Algorithm 1: Self-Shadowing Checking

input : A^{T}, A^{R}, and body part set $\mathcal{P}$
output: $\mathcal{C}$

Initialization: $\mathcal{C} \leftarrow \{1, 2, ..., P\}$;
for $i = 1 : \texttt{size}(\mathcal{P})$ **do**
  $dir_1 = A^{\mathrm{T}} - \mathcal{P}(i, 1:3)$;
  $dir_2 = A^{\mathrm{R}} - \mathcal{P}(i, 1:3)$;
  for $j = \{1 : \texttt{size}(\mathcal{P})\} \backslash i$ **do**
    $bbox = \texttt{ComputeBox}(\mathcal{P}(j))$;
    $dir_t = A^{\mathrm{T}} - \mathcal{P}(j, 1:3)$;
    $dir_r = A^{\mathrm{R}} - \mathcal{P}(j, 1:3)$;
    if $(\texttt{norm}(dir_1) > \texttt{norm}(dir_t))$ & $(\texttt{norm}(dir_2) > \texttt{norm}(dir_r))$ **then**
      if $\texttt{IsIntersct}(bbox, A^{\mathrm{T}}, dir_1)$ & $\texttt{IsIntersct}(bbox, A^{\mathrm{R}}, dir_2)$ **then**
        if $\texttt{IsIntersct}(\mathcal{P}(j), A^{\mathrm{T}}, dir_1)$ & $\texttt{IsIntersct}(\mathcal{P}(j), A^{\mathrm{R}}, dir_2)$ **then**
          $\mathcal{C} \leftarrow \mathcal{C} \backslash j$;
          break;
Return: $\mathcal{C}$

We adopt micro-Doppler as a signature of various human activities and the spectrogram $S(f,t)$ is plotted for identification. The micro-Doppler extraction process is summarized in the following:

- Integrating complex channel gain over propagation delay τ' from 0 to $\tau_{\max}$ as $\mu(t)$.
- Conduct short-time Fourier transform (STFT) on $\mu(t)$ as
$$X(f,t) = \int_{-\infty}^{\infty} \mu(t) w(t'-t)\, e^{-i2\pi f t'} dt', \qquad (20)$$
where $\omega(t)$ is a window function.
- Finally, the spectrogram $S(f,t) = |X(f,t)|^2$.

IV. Simulation and Analysis

In this section, we present simulation results of the established channel model for human activity sensing. We first give a workflow for simulating human activities. To further facilitate the model into the concept of ISAC, we adopt the orthogonal frequency-division multiplexing (OFDM) waveform in the following simulations, and the implementation of OFDM waveform in the channel model is introduced. Micro-Doppler is selected as a major signature for depicting human activity simulations with channel models. Simulations for micro-Doppler signatures of various human activities under monostatic and bistatic configurations are demonstrated. Finally, we introduce the measurements for human activity sensing, and the comparison between simulation results and measurement results is included.

A. Simulation Workflow

For the indoor scenario, we consider a 3m×3m×3m cube, and transceivers, background scatterers, and moving scatterers indicating the human body should be placed within the space. Figure 4 depicts the workflow of simulating human activities with the proposed scattering channel model, which contains the following 3 parts.

1) Signal transmitting

As introduced above, the antenna pattern can be adjusted in this simulation. Besides, antenna array parameters such as antenna number, polarization, etc., can be determined. Then, we define the OFDM waveform with customized parameters such as the number of subcarriers, OFDM symbol duration, etc., and then the quadrature amplitude modulation (QAM) is conducted to generate OFDM samples. The sensing signal is finally transmitted after defining Tx's antenna and peak power.

2) Sensing channel

The sensing channel includes moving human target scattering and fixed cluster scattering model. For the human target model [7], we obtain MOCAP data from the existing dataset at first. Second, we can extract the position vector of each scattering point, where the human movement is indicated by the position vector dataflow at the video frame rate of the point cloud. Then, we fit a human skeleton model to a point cloud, which is built by a series of reference points indicating critical joints of the human body. Then, we embody the human skeleton with primitives to estimate the RCS of each body part over time. State that here we need to interpolate the data at the sensing sampling frequency. For the cluster-based scattering model, we generate the distance and angle information of background scatterers following the ellipsoid

$$\begin{cases} \sigma^{\mathrm{H}}_{ij,p}(t) = \dfrac{\pi a_p^2 b_p^2 c_p^2 \Theta^{\mathrm{S}}_p}{\left(a_p^2 \Phi^{\mathrm{S}}_p + b_p^2 \Psi^{\mathrm{S}}_p + c_p^2 (\cos\varphi^{\mathrm{EOA}}_{ij,p}(t) + \cos\varphi^{\mathrm{EOD}}_{ij,p}(t))^2\right)^2} \\ \Theta^{\mathrm{H}}_{ij,p} := ((1 + \cos\varphi^{\mathrm{EOA}}_{ij,p}(t)\cos\varphi^{\mathrm{EOD}}_{ij,p}(t)) \cdot \cos(\varphi^{\mathrm{AOA}}_{ij,p}(t) - \phi^{\mathrm{S}}_p(t)) + \sin\varphi^{\mathrm{EOA}}_{ij,p}(t)\sin\varphi^{\mathrm{EOD}}_{ij,p}(t))^2 \\ \Phi^{\mathrm{H}}_{ij,p} := (\sin\varphi^{\mathrm{EOD}}_{ij,p}(t)\cos\varphi^{\mathrm{AOD}}_{ij,p}(t) + \sin\varphi^{\mathrm{EOA}}_{ij,p}(t)\cos\varphi^{\mathrm{AOA}}_{ij,p}(t))^2 \\ \Psi^{\mathrm{H}}_{ij,p} := (\sin\varphi^{\mathrm{EOD}}_{ij,p}(t)\sin\varphi^{\mathrm{AOD}}_{ij,p}(t) + \sin\varphi^{\mathrm{EOA}}_{ij,p}(t)\sin\varphi^{\mathrm{AOA}}_{ij,p}(t))^2 \end{cases}, \qquad (17)$$

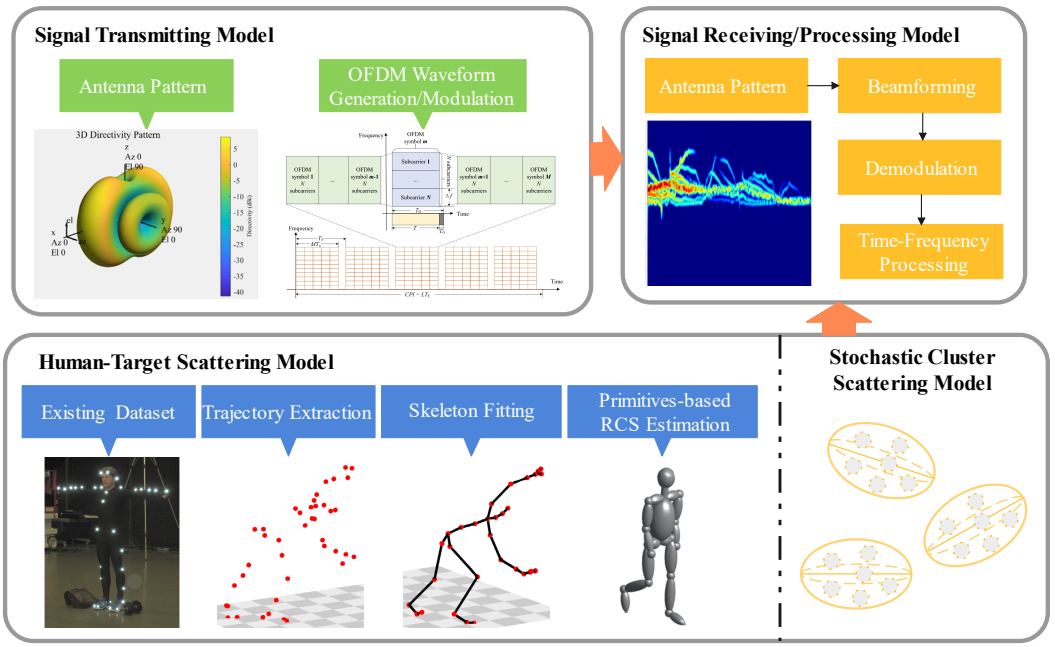

FIGURE 4. **Simulation workflow of human activity sensing.**

Gaussian scattering model, and the number of paths varies with time.

3) Received signal

At the Rx side, antenna pattern, antenna array, noise figure, etc., are determined. According to the trajectory of each body part, we calculate delay and Doppler based on position change over time; together with RCS, we can finally build the scattering signal for the human target. Adding signal scattering from fixed clusters and double-bounces from both moving and background scatterers, the received signal is formulated. For OFDM waveform, the attenuated, delayed, and Doppler shifted signal from the human target is given as [23]

$$(\mathbf{F}_{\mathrm{Rx}})_{ij,uv} = \sum_{p=1}^{P} G_{ij,p} a_{ij,p}^{\mathrm{H}} (\mathbf{F}_{\mathrm{Tx}})_{ij,uv} \cdot \exp\left[j2\pi v T_O f_{ij,p}^{\mathrm{H}}\right], \quad (21)$$
$$\cdot \exp\left[-j2\pi\tau_{ij,p}^{\mathrm{H}}(u\Delta f + f_c)\right] + (\mathbf{Z})_{ij,uv}$$

where $\mathbf{F}_{\mathrm{Tx}}$, $\mathbf{F}_{\mathrm{Rx}}$, and $\mathbf{Z}$ indicate transmitted OFDM frame, received OFDM frame, and noise, respectively, where each row and column represent a sub-carrier and an OFDM symbol with u and v denoting indexes, and T_O represents the whole OFDM duration. After beamforming and demodulation at the Rx, the received signal is deducted from the transmitted signal. At last, the derived channel matrix is conducted with STFT to obtain micro-Doppler signatures.

B. Simulation Configuration

For both Tx and Rx, we adopted a uniform linear array (ULA) with 4 short dipole antenna elements, where the spacing between each element is half the wavelength. Thus, the simulated array gain is 8.74dBi. For the OFDM waveform, we select parameters according to the range/velocity resolution requirements for human activity sensing. For a determined range resolution Δr, the minimum bandwidth $B = c/(2\Delta r)$ should be satisfied. For OFDM symbols, the symbol duration is reciprocal of the separation between OFDM subcarriers, and the duration of the cyclic prefix (CP) relies on the maximum detected range $r_{\max}$ as $T_{\mathrm{cp}} = 2r_{\max}/c$. Besides, velocity resolution is determined by the window size of STFT and the maximum detectable velocity is determined by the packet repetition frequency. Stated that for various human activities, we use a dataset [12] from the MOCAP system where the video frame rate is not sufficient for human moving velocity; thus, we interpolate the video frame to make sure that the sampling frequency is not lower than 1kHz. For cluster generation, $\varepsilon_{DS} = 1.1, \varepsilon_{AS} = 1.4, \varepsilon_{ES} = 1.4$ are used in the simualtion to indicate an indoor room [21]. Detailed parameters of the simulation can be found in Table 1.

C. Micro-Doppler Signature

In this subsection, we present micro-Doppler signatures of different human motions. At first, we plot micro-Doppler features with our proposed simulation without multi-path scattering from the indoor environment, i.e., neglecting the background scatterers effect, under both monostatic and bistatic deployments. Then, we depict micro-Doppler signatures with consideration of fixed clusters as well as second bounces. Finally, we present a measurement dataset on human activities and compare results from both simulation and measurements. Stated that for both monostatic and

This article has been accepted for publication in IEEE Open Journal of Antennas and Propagation. This is the author's version which has not been fully edited and content may change prior to final publication. Citation information: DOI 10.1109/OJAP.2024.3516533

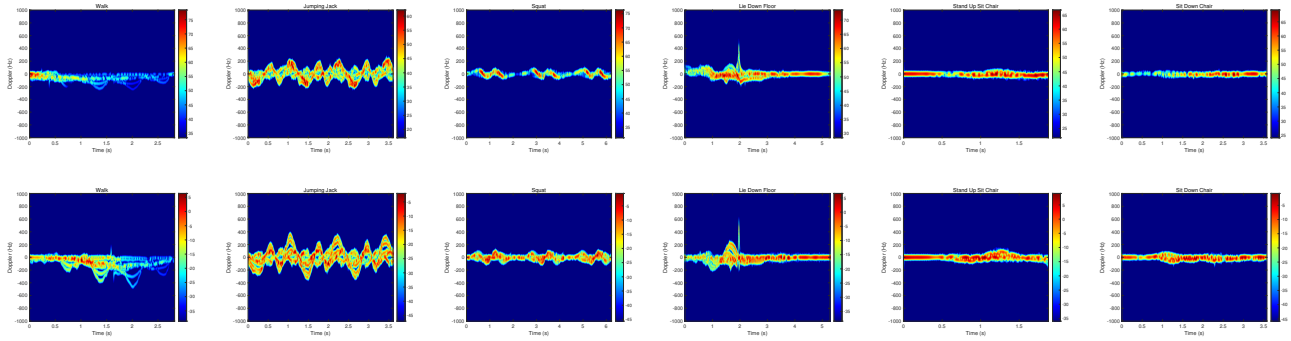

FIGURE 5. **Micro-Doppler signatures of human walk, jump jack, squat, lie down floor, stand up from chair, and sit down chair under monostatic (first row) and bistatic (second row) deployments.**

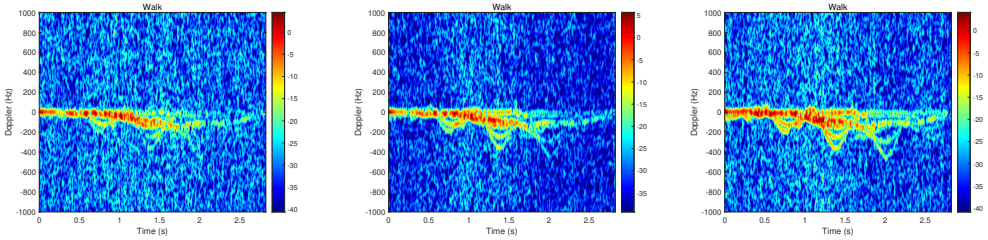

(a) $\beta = 60°$ (b) $\beta = 90°$ (c) $\beta = 120°$

FIGURE 6. **Micro-Doppler signatures of human walking with consideration of cluster-based environment scattering and second bounces.**

TABLE 1. **Parameter for HAR Simulation**

Parameter	Symbol	Value
Carrier frequency	f_c	28GHz
Bandwidth	B	5GHz
Number of subcarriers	N	1024
Duration of a symbol	T	0.20μs
Duration of cyclic prefix	$T_{\rm cp}$	0.07μs
Total OFDM duration	T_O	0.27μs
Turn-off duration between frames	$\rm T_{off}$	2.35μs
Packet repetition interval	$P_{\rm F}$	15.59μs
Packet repetition frequency	PRF	2kHz
Bits per QAM symbol	bps	6
Peak power of Tx	P_t	0.01W
Pwer amplifier (PA) gain	$G_{\rm tx}$	5dB
Low noise amplifier (LNA) gain	$G_{\rm rx}$	5dB
Rx noise figure	NF	2.9dB
Maximum detectable range	$r_{\max}$	10m
Range resolution	Δr	3cm

bistatic deployment, the sensing target, i.e., the human body, stands at the original coordinate $[0, 0, 0]$. For monostatic deployment, the Tx/Rx coordinate is $[0, 0.9, -1]$, and the azimuth and elevation angle vector is presented in a vector as $[0, 0]$. For bistatic deployment, Tx and Rx are located at $[0, 0.9, 1]$ with angle vector $[45, 0]$ and $[0, 0.9, -1]$ with angle vector $[-45, 0]$, respectively.

1) Micro-Doppler Signatures without Background Clusters

Figure 5 depicts micro-Doppler signatures of human walk, jump jack, squat, lie down floor, stand up from chair, and sit down on chair, where the first row shows results under monostatic deployment and the second row under bistatic deployment. Using our simulation, only one human is considered as the target and only scattering from the human body is included in the channel part. Due to the micro-motions of different body parts, micro-Doppler features can indicate the particular human's motions, which we can utilize for motion or activity identification and classification. Stated that Fig. 5 only shows some exemplary human motions by one actor from the database. However, the database contains more samples, and spectrogram segmentation can be conducted to obtain more data for algorithms such as machine learning.

2) Micro-Doppler Signatures with Background Clusters and Second Bounces

With consideration of the cluster-based environment scattering model and second bounces, we present micro-Doppler signatures for human walking under bistatic deployment as in Fig. 6. Here we set $\lambda_B = 25/\text{m}$ and $\lambda_D = 5/\text{m}$ and the initial number of both $C^{\rm F}$ and $C^{\rm L}$ are 5, within which 5 scatterers are contained. Through the simulation, we found that even with the birth-death process, the human body moving will not cause the obvious change in the background cluster number at each time instant. Here we depict the impact of the bistatic angle on micro-Doppler

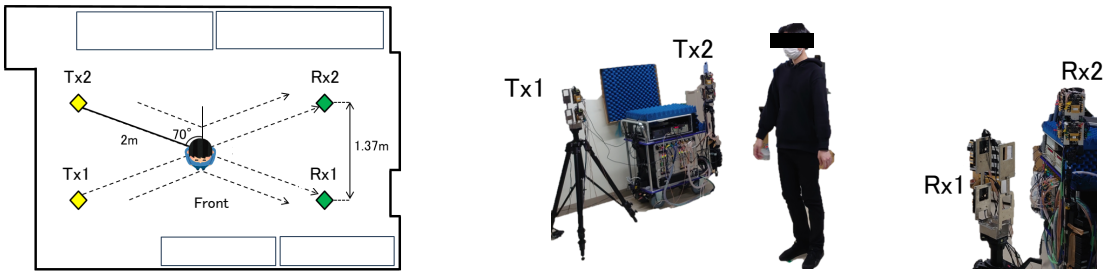

(a) Multi-static measurement schematic (b) Hardware deployment

FIGURE 7. **Measurement system configuration.**

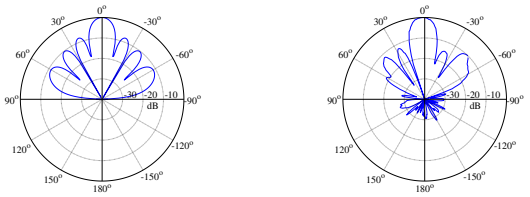

(a) (b)

FIGURE 8. **Comparison of beam pattern generated by (a) simulation and (b) measurement.**

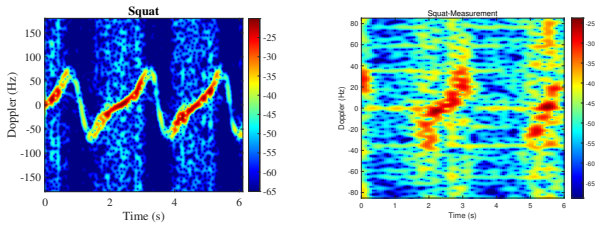

(a) (b)

FIGURE 9. **Comparison between (a) simulated and (b) measured micro-Doppler signature under human squat.**

signatures, where Fig. 6 (a-c) presents human waking with bistatic angle $\beta = 60°$, $90°$, and $120°$, respectively. We can conclude that with $\beta = 120°$, the micro-Doppler signature is more detectable, which also relies on target's orientation and location. With $\beta = 60°$, signatures became vague as the human walks away.

D. Measurements Comparison

We compare simulation results using our proposed channel model with a measurement dataset on human activity sensing by Niigata University. The hardware configuration of the double-directional channel sounder, utilizing a commercial-off-the-shelf phased-array beamformer, is detailed in [24], [25]. Figure 7 depicts the configuration of the measurement setup. In this experiment, the antennas are placed in four locations with Tx of 2 and Rx of 2 with a height of 1.4m. The distance between Tx1-Tx2 and Rx1-Rx2 is 1.37m, respectively, and the distance between Tx1-Rx1 and Tx2-Rx2 is 1.88m, respectively. The target, i.e., a human, stands in the center of four antennas arranged in a rectangular shape. The distance from each antenna to the target is 2m, and the Tx-target-Rx propagation distance is 4m. Channel responses with multiple human activities are measured with sampling frequency 170Hz and for each scenario, four channels, i.e., Tx1-Rx1, Tx1-Rx2, Tx2-Rx1, and Tx2-Rx2 are obtained. The frequency of the transmitting signal is 24.15 GHz. In the measurements, 2×8 planar antenna arrays are utilized at both Tx and Rx. Similarly, in the simulations, we apply uniform rectangular arrays (URA) with 2×8 short dipole antenna elements. To match the 32dBm equivalent isotropic radiated power (EIRP) in measurements, we set Tx peak power $P_t = 7.84$dBm and PA gain $G_{\text{tx}} = 5$dB as the antenna array gain is 14.16dBi in simulations. To better reflect the real system's characteristics, we set LNA gain to $G_{\text{rx}} = 5$dB and noise figure to 2.9dB, ensuring that the received signal power aligns with the levels observed in measurements. Further detailed parameters on the transceivers used in the measurement are listed in Table 2.

TABLE 2. **Parameter for Transceiver in Measurement**

Parameter	Symbol	Value
Carrier frequency	f_c	24.15GHz
Bandwidth	B	100MHz
Number of subcarriers	N	512
Sampling rates	f_s	400Msps
Range resolution	Δr	150cm
Delay span	T_{cp}	2.56μs
EIRP of Tx	EIPR	32dBm

To accommodate the testbed, we deploy the bi-static transmitter and receiver with the same location as Tx2-Rx2 link as in Fig. 7 during the simulation. The carrier frequency is set as 24.15 GHz. The initial number of both C^{F} and C^{L} are 5, within which 5 scatterers are included to simulate the indoor environment. In the measurement, due to the low sampling frequency, it is not possible to generate micro-Doppler signatures of human motions with higher velocity. However, there are lower-velocity motions such as squatting and walking on the spot, which we chose as samples for comparison. In the simulation, we adopted a sampling frequency of 360Hz to capture micro-Doppler

signatures of the human motion from the MOCAP dataset. A comparison of beam patterns generated by simulation and measurement is depicted in Fig. 8. According to [24], the transmitter consists of four antenna arrays to cover the 360° field of view, while for the measured channel, only one antenna array is used. Hence, we plot a diagram of the antenna array patterns to show the consistency of simulation and measurement configuration. The envelopes and the power of the two patterns are consistent.

Figure 9 (a) depicts the simulated micro-Doppler signature of human squat with our proposed channel model. After conducting STFT on channel data (channel Tx2-Rx2) and fixed scattering removal, we also obtained the micro-Doppler signatures of the human squat as in Fig. 9 (b) from measurements. The forms of micro-Doppler signatures show similarity. Due to the unaltered human moving speed in the MOCAP dataset as well as in the completed measurement dataset, the maximum Doppler shown in simulated micro-Doppler signatures is not strictly aligned with that from the measurements. However, the envelope and form of the signatures from simulation and measurement demonstrate generally good agreement.

The comparison between Fig. 5 and Fig. 6 demonstrates the effect of integrating the environment cluster model and the self-shadowing checks in the proposed model. During the numerical analysis, micro-Doppler signatures for various human activities are derived within 10 minutes using standard laptops, eliminating the need for input frames of human animation as required by ray-tracing-based models, thereby saving both time and computational resources. Besides, the proposed model and experimental demonstrations can be extended to other domains. For instance, in gesture recognition, this model can be used to analyze fine movements of the hand, enabling precise identification of gestures. This is particularly relevant for human-computer interaction systems in AR environments, where detecting and interpreting gestures in real-time is crucial for seamless interaction. The model's ability to accurately capture micro-Doppler signatures of human motion makes it suitable for these applications, and further optimizations could ensure that it meets the efficiency and accuracy requirements of these emerging fields.

V. Conclusions

Our work presents a novel approach to model the indoor mmWave scattering channel. By integrating primitive-based and cluster-based scattering models, we have developed a refined channel model that efficiently considers self-shadowing and double-bounce environment scattering, crucial for accurate HAR performance. Additionally, we have constructed a comprehensive simulation framework facilitating system design and optimization. We have validated the effectiveness of our proposed approach through comparative experiments with real-world measurements, demonstrating that the proposed work mitigates the tradeoff between the time-consuming and modeling accuracy of existing works, where most human activities can be identified with micro-Doppler signatures within 10 minutes. The significance of our work lies in its potential to advance the utilization of mmWave technology for HAR applications in emerging 6G networks, addressing the increasing demand for precise human activity sensing across various sectors.

REFERENCES

[1] H. Zhang, D. Wang, S. Wu, W. Guan, and X. Liu, "USTB 6G: Key technologies and metaverse applications," *IEEE Wireless Commun.*, vol. 30, no. 5, pp. 112–119, Oct. 2023.

[2] S. Faghih-Naini, C. Sebastian, T. Reissland, R. Weigel, and B. Scheiner, "Hardware design challenges and modulation schemes in joint communication and sensing: Analyzation and comparison of the state-of-the-art co-located communication and sensing systems," *IEEE Microw. Mag.*, vol. 25, no. 3, pp. 84–97, Mar. 2024.

[3] B. Fu, N. Damer, F. Kirchbuchner, and A. Kuijper, "Sensing technology for human activity recognition: A comprehensive survey," *IEEE Access*, vol. 8, pp. 83 791–83 820, May 2020.

[4] J. Zhang, R. Xi, Y. He, Y. Sun, X. Guo, W. Wang, X. Na, Y. Liu, Z. Shi, and T. Gu, "A survey of mmWave-based human sensing: Technology, platforms and applications," *IEEE Commun. Surv. Tutorials.*, vol. 25, no. 4, pp. 2052–2087, Jul. 2023.

[5] J. Lien, N. Gillian, M. E. Karagozler, P. Amihood, C. Schwesig, E. Olson, H. Raja, and I. Poupyrev, "Soli: Ubiquitous gesture sensing with millimeter wave radar," *ACM Trans. Graph.*, vol. 35, no. 4, Jul. 2016.

[6] T. Incorporeted, "Single-chip 76-GHz to 81-GHz automotive radar sensor integrating MCU and hardware accelerator," 2020. [Online]. Available: https://www.ti.com/product/AWR1443

[7] S. Vishwakarma, W. Li, C. Tang, K. Woodbridge, R. Adve, and K. Chetty, "SimHumalator: An open-source end-to-end radar simulator for human activity recognition," *IEEE Aerosp. Electron. Syst. Mag.*, vol. 37, no. 3, pp. 6–22, Mar. 2022.

[8] K. Yang, Q. H. Abbasi, F. Fioranelli, O. Romain, and J. Le Kernec, "Bespoke simulator for human activity classification with bistatic radar," in *16th EAI International Conference on Body Area Networks, BODYNETS 2021*, Virtual, Online, 25-26 Dec. 2021, pp. 71–85.

[9] F. Firdaus, N. A. Ahmad, and S. Sahibuddin, "Accurate indoor-positioning model based on people effect and ray-tracing propagation," *Sensors*, vol. 19, no. 24, Dec. 2019.

[10] K. D. Trott, "Stationary phase derivation for RCS of an ellipsoid," *IEEE Antennas Wirel. Propag. Lett.*, vol. 6, pp. 240–243, Jun. 2007.

[11] Z. Cao, G. Hidalgo, T. Simon, S. Wei, and Y. Sheikh, "OpenPose: Realtime multi-person 2D pose estimation using part affinity fields," *IEEE Trans. Pattern Anal. Mach. Intell.*, vol. 43, no. 1, pp. 172–186, Jan. 2021.

[12] M. Müller, T. Röder, M. Clausen, B. Eberhardt, B. Krüger, and A. Weber, "Documentation mocap database HDM05," Universität Bonn, Tech. Rep. CG-2007-2, Jun. 2007.

[13] B. Erol and S. Z. Gurbuz, "A kinect-based human micro-Doppler simulator," *IEEE Aerosp. Electron. Syst. Mag.*, vol. 30, no. 5, pp. 6–17, May 2015.

[14] J. Pegoraro, J. O. Lacruz, F. Meneghello, E. Bashirov, M. Rossi, and J. Widmer, "RAPID: Retrofitting IEEE 802.11ay Access Points for Indoor Human Detection and Sensing," *IEEE Trans. Mob. Comput.*, pp. 1–18, Jul. 2023.

[15] H. Zhao, Q. Wang, K. Shi *et al.*, "Analysis on human blockage path loss and shadow fading in millimeter-wave band," *Int. J. Antennas Propag.*, vol. 2017, no. 1, p. 7540202, Aug. 2017.

[16] M. Arnold, M. Bauhofer, S. Mandelli, M. Henninger, F. Schaich, T. Wild, and S. ten Brink, "Maxray: A raytracing-based integrated sensing and communication framework," in *2022 2nd IEEE International Symposium on Joint Communications & Sensing (JC&S)*, Seefeld, Austria, 09-10 Mar. 2022, pp. 1–7.

[17] J. Ebrahimizadeh, A. Madannejad, X. Cai, E. Vinogradov, and G. A. E. Vandenbosch, "RCS-based 3-D millimeter-wave channel modeling using quasi-deterministic ray tracing," *IEEE Trans. Antennas Propag.*, vol. 72, no. 4, pp. 3596–3606, Feb. 2024.

[18] N. Avazov, R. Hicheri, and M. Pätzold, "Micro-Doppler characteristics of mmWave indoor backscattering channels for RF sensing," in *2022*

18th International Conference on Wireless and Mobile Computing, Networking and Communications (WiMob), Thessaloniki, Greece, 10-12 Oct. 2022, pp. 357–362.

[19] N. Avazov, R. Hicheri, and M. Ptzold, "A trajectory-driven SISO mm-Wave channel model for a human activity recognition," in *2021 17th International Conference on Wireless and Mobile Computing, Networking and Communications (WiMob)*, Bologna, Italy, 11-13 Oct. 2021, pp. 133–138.

[20] N. Avazov, R. Hicheri, M. Muaaz, F. Sanfilippo, and M. Pätzold, "A trajectory-driven 3D non-stationary mm-Wave MIMO channel model for a single moving point scatterer," *IEEE Access*, vol. 9, pp. 115 990–116 001, Aug. 2021.

[21] J. Bian, C.-X. Wang, X. Gao, X. You, and M. Zhang, "A general 3D non-stationary wireless channel model for 5G and beyond," *IEEE Trans. Wirel. Commun.*, vol. 20, no. 5, pp. 3211–3224, Jan. 2021.

[22] R. Yang, C.-X. Wang, J. Huang, E.-H. M. Aggoune, and Y. Hao, "A novel 6G ISAC channel model combining forward and backward scattering," *IEEE Trans. Wirel. Commun.*, vol. 22, no. 11, pp. 8050–8065, Nov. 2023.

[23] M. Liu, F. Gao, Z. Cui, S. Pollin, and Q. Liu, "Sensing with OFDM waveform at mmWave band based on micro-Doppler analysis," in *2023 IEEE International Conference on Communications Workshops (ICC Workshops)*, Rome, Italy, 28 May - 1 June 2023, pp. 1398–1403.

[24] M. Kim, H. Tsukada, K. Kumakura, R. Takahashi, N. Suzuki, H. Sawada, and T. Matsumura, "A 24/60-GHz dual-band double-directional channel sounder using COTS phased arrays," in *2022 IEEE International Conference on Communications Workshops (ICC Workshops)*, Seoul, Korea, Republic of, 16-20 May 2022, pp. 1113–1117.

[25] M. Kim, H. Pham, Y. Chang, and J. ichi Takada, "Development of low-cost 60-GHz millimeter-wave channel sounding system," in *6th Global Symposium of Millimeter Waves (GSMM 2013))*, Sendai, Japan, Apr. 2013.

MINGQING LIU received the B.S. degree in computer science and technology from the Northwest A&F University, Yangling, China, in 2018, and her Ph.D. degree with the College of Electronics and Information Engineering, Tongji University, Shanghai, China, in 2024. She is currently working as a postdoctoral research associate in Li-Fi Research and Development Centre, University of Cambridge, Cambridge, UK. Her research interests lie in the areas of wireless power transfer, simultaneous lightwave information and power transfer, integrated communication and positioning, and the Internet of Things.

ZHUANGZHUANG CUI (Member, IEEE) received the Ph.D. degree in Electrical Engineering from the Beijing Jiaotong University, Beijing, China, in April 2022. Currently, he is a postdoctoral research associate with the Networked Systems group at KU Leuven, Belgium. He serves as a co-chair of the 3rd ACM MobiCom'23 Workshop on ISAC and co-chair of the IEEE ICCC'24 workshop on data-model integration for wireless advances. He is the recipient of the National Scholarship from China in 2020, and Postdoctoral Mandate from KU Leuven in 2022. His research interests include channel modeling, UAV, and ISAC.

YANG MIAO (Senior Member, IEEE and URSI) received the M.Sc. and Ph.D. degrees from the Radio Propagation Laboratory, Mobile Communications Research Group, Tokyo Institute of Technology, Tokyo, Japan, in 2012 and 2015, respectively. From 2010 to 2015, she was a Research Assistant with the Takada Laboratory, Tokyo Institute of Technology. From 2015 to 2018, she was a Post-Doctoral Researcher with the Institute of Information and Communication Technologies, Electronics, and Applied Mathematics, Universite Catholique de Louvain, Louvain-la-Neuve, Belgium, and IMEC, Wireless, Acoustics, Environment, and the Expert Systems Laboratory, Ghent University, Ghent, Belgium. From 2017 to 2018, she was a part-time Senior Antenna Engineer with Jaguar Radio Wave Corporation, Shenzhen, China. From 2018 to 2019, she was a Research Assistant Professor at the Southern University of Science and Technology, Shenzhen. From Aug. 2019 to May 2024 she was an Assistant Professor and from June 2024 she is an Associate Professor with the Radio Systems Group, University of Twente, 4TU, The Netherlands. Since November 2021, she has also been affiliated part-time with KU Leuven, Leuven, Belgium, as a Marie Curie Individual Fellow. Her research interests include joint communication and sensing, incorporating mobility, and human factors.

MINSEOK KIM (Senior Member, IEEE) received a B.S. degree in Electrical Engineering from Hanyang University, Seoul, Korea, and his M.E. and D.E. degrees in the Division of Electrical and Computer Engineering, Yokohama National University (YNU), Japan in 1999, 2002, and 2005, respectively. In 2007, he was an Assistant Professor with the Tokyo Institute of Technology, Tokyo, Japan, and a Visiting Scholar with the Georgia Institute of Technology, Atlanta, GA, USA, in 2010. In 2014, he joined the Graduate School of Engineering, Niigata University, Niigata, Japan, as an Associate Professor.

His current research interests include radio propagation channel measurement and modeling for various wireless systems, millimeter-wave radar, radio-based localization, and MIMO/antenna array signal processing. He is a Senior Member of the IEICE. He is also serving as an Associate Editor for *IEEE Access* and *IEEE Antennas Wirel. Propag. Lett.*.

SOFIE POLLIN (Senior Member, IEEE) is a Professor with KU Leuven focusing on wireless communication systems. Before that, she worked with imec and the University of California at Berkeley, and she is currently a Principal Member of the technical staff at imec. Her research centers around wireless networks that require networks that are ever more dense, heterogeneous, battery-powered, and spectrum-constrained. Her research interests are cell-free networks, integrated communication and sensing, and non-terrestrial networks.